arXiv:1411.2254v1 [astro-ph.HE] 9 Nov 2014

A detailed X-ray investigation of PSR J2021+4026 and $\gamma-$Cygni supernova remnant

C. Y. Hui[1], K. A. Seo[1], L. C. C. Lin[2], R. H. H. Huang[2], C. P. Hu[3], J. H. K. Wu[2], L. Trepl[4], J. Takata[5], Y. Wang[5], Y. Chou[3], K. S. Cheng[5] and A. K. H. Kong[2]

cyhui@cnu.ac.kr

Received _____; accepted _____

[1]Department of Astronomy and Space Science, Chungnam National University, Daejeon, Republic of Korea

[2]Institute of Astronomy and Department of Physics, National Tsing Hua University, Hsinchu, Taiwan

[3]Graduate Institute of Astronomy, National Central University, Jhongli 32001, Taiwan

[4]Astrophysikalisches Institut und Universitäts-Sternwarte, Universität Jena, Schillergäβchen 2-3, 07745 Jena, Germany

[5]Department of Physics, University of Hong Kong, Pokfulam Road, Hong Kong

ABSTRACT

We have investigated the field around the radio-quiet γ-ray pulsar, PSR J2021+4026, with a $\sim$ 140 ks *XMM-Newton* observation and a $\sim$ 56 ks archival *Chandra* data. Through analyzing the pulsed spectrum, we show that the X-ray pulsation is purely thermal in nature which suggests the pulsation is originated from a hot polar cap with $T \sim 3 \times 10^6$ K on the surface of a rotating neutron star. On the other hand, the power-law component that dominates the pulsar emission in the hard band is originated from off-pulse phases, which possibly comes from a pulsar wind nebula. In re-analyzing the *Chandra* data, we have confirmed the presence of bow-shock nebula which extends from the pulsar to west by $\sim$ 10 arcsec. The orientation of this nebular feature suggests that the pulsar is probably moving eastward which is consistent with the speculated proper motion by extrapolating from the nominal geometrical center of the supernova remnant (SNR) G78.2+2.1 to the current pulsar position. For G78.2+2.1, our deep *XMM-Newton* observation also enables a study of the central region and part of the southeastern region with superior photon statistics. The column absorption derived for the SNR is comparable with that for PSR J2021+4026, which supports their association. The remnant emission in both examined regions are in an non-equilibrium ionization state. Also, the elapsed time of both regions after shock-heating is apparently shorter than the Sedov age of G78.2+2.1. This might suggest the reverse shock has reached the center not long ago. Apart from PSR J2021+4026 and G78.2+2.1, we have also serendipitously detected an X-ray flash-like event XMM J202154.7+402855 from this *XMM-Newton* observation.

Subject headings: stars:neutron — pulsars:individual: PSR J2021+4026 (2XMM J202131.0+402645) — supernovae:individual: G78.2+2.1($\gamma-$Cygni)

1. INTRODUCTION

The Cygnus region, which locates at $\sim 80^{\circ}$ from the Galactic center, is one of the most complex $\gamma-$ray structure on the Galactic plane. Many interesting sources are found to reside in this region, including OB association, microquasar, supernova remnants and rotation-powered pulsars. Since the launch of the *Fermi* Gamma-Ray Space Telescope, many new $\gamma-$ray pulsars have been uncovered in the Cygnus region either in blind searches or by folding the $\gamma-$ray data with the timing ephemeris determined through radio observations (Abdo et al. 2013). Among them, the most intriguing one is PSR J2021+4026, which belongs to the growing class of radio-quiet γ-ray pulsars.

PSR J2021+4026 is a bright γ-ray source which was detected at a significance $> 10\sigma$ with only the first 3 months LAT data (Abdo et al. 2009a 0FGL). Its timing ephemeris was subsequently reported (Abdo et al. 2009b, 2010). It has a rotation period and first period derivative of $P = 265$ ms and $\dot{P} = 5.48 \times 10^{-14}$ s s^{-1} respectively, which imply a spin-down age of ~ 77 kyr, surface dipolar magnetic field strength of $\sim 4 \times 10^{12}$ G and a spin-down power of $\sim 10^{35}$ erg s^{-1}.

Recently, the long-term $\gamma-$ray monitoring of PSR J2021+4026 has discovered its $\gamma-$ray flux at energies > 100 MeV has suddenly decreased by $\sim 18\%$ near MJD 55850 (Allafort et al. 2013). This flux jump was accompanied by the change in the $\gamma-$ray pulse profile and the spin-down rate. These make PSR J2021+4026 to be the first variable $\gamma-$ray pulsar has ever been observed.

Despite the efforts devoted in searching for its radio counterpart, no radio pulsar associated with PSR J2021+4026 has been detected so far (Becker et al. 2004; Trepl et al. 2010; Ray et al. 2011). Without radio detection, observations in X-ray regime is particularly important for constraining the emission nature of radio-quiet γ-ray pulsars. Soon after the detection of PSR J2021+4026 has been reported by Abdo et al. (2009a), we have searched

for its X-ray counterpart by using all the avaliable archival data (Trepl et al. 2010). Within the 95% confidence circle of PSR J2021+4026 at that time (0FGL J2021.5+4026; cf. Abdo et al. 2009a), we reported the identification of the X-ray source 2XMM J202131.0+402645 / CXOU 202130.55+402646.9 from the *XMM-Newton* (ObsID: 150960801) and *Chandra* (ObsID: 5533) data as the possible counterpart of PSR J2021+4026. This source was found to be the only non-variable X-ray object without any optical/IR counterpart within the γ-ray error circle. The association between the pulsar and this source is reinforced by the fact that the X-ray position is consistent with the optimal γ-ray timing solution (Trepl et al. 2010). These results have been confirmed by a follow-up 56 ks *Chandra* observation for a dedicated investigation (ObsID 11235; Weisskopf et al. 2011). This observation also enables the authors to examine the X-ray spectrum of this promising counterpart of PSR J2021+4026 and found that it possibly contains both thermal and non-thermal contributions.

Although all the aforementioned investigations strongly suggest the association between 2XMM J202131.0+402645 and PSR J2021+4026, the physical connection between this X-ray source and the γ-ray pulsar could not be confirmed unambiguously until the X-ray pulsation was recently discovered by us with a deep *XMM-Newton* observation (Lin et al. 2013). The consistency between the detected X-ray periodicity and the $\gamma-$ray pulsation at the same epoch has eventually nailed down the long-sought connection between 2XMM J202131.0+402645 and PSR J2021+4026. In this paper, we reported a further X-ray analysis of PSR J2021+4026 by disentangling its pulsed and unpulsed components. Also, by re-examining archival on-axis *Chandra* observation, we have searched for the possible pulsar wind nebula around PSR J2021+4026.

Apart from PSR J2021+4026, our *XMM-Newton* observation also covers the central region and part of the southeastern rim of the supernova remnant (SNR) $\gamma-$Cygni

(G78.2+2.1) which has been suggested to be associated with PSR J2021+4026 (Trepl et al. 2010). G78.2+2.1 is rather extended. Its radio and X-ray shells have a size of $\sim 1^\circ$ (Leahy, Green & Ranasinghe 2013). The X-ray emission from G78.2+2.1 has been investigated several times with *ROSAT*, *ASCA* and *Chandra* (Lozinskaya et al. 2000; Uchiyama et al. 2002; Aliu et al. 2013; Leahy et al. 2013). The most recent X-ray imaging spectroscopic analysis of G78.2+2.1 is reported by Leahy et al. (2013). By using the archival *Chandra* data, the authors have examined the diffuse X-ray emission from the northern part and the central region of G78.2+2.1. While the column absorption for these two spatial regions are found to comparable, the plasma temperature of the central region, $\sim 10^7$ K, is suggested to be higher. However, the uncertainties of the spectral parameters are too large for drawing a firm conclusion. This is can be ascribed to the low surface brightness of the central region (see Fig. 4 in Leahy et al. 2013) and the relatively inferior collecting power of *Chandra*.

For the southeastern rim, it contributes $\sim 60\%$ of the radio flux of this SNR which is known as DR4 (Downes & Rinehart 1966). While this is the brightest part in radio, it is very dim in X-ray regime (see Fig. 1 in Uchiyama et al. 2002). This part has been excluded in the updated investigation by Leahy et al. (2013), as there is no existing *Chandra* data that covers this region. With our deep *XMM-Newton* observation, we are able to provide tighter constraints on the emission nature of the central and southeastern part of G78.2+2.1 and its possible association with PSR J2021+4026.

2. OBSERVATION & DATA ANALYSIS

2.1. Observations & Data Reduction

Our deep *XMM-Newton* observation of the field around PSR J2021+4026 started on 2012 April 11 with a total on-time of 135.8 ks (ObsID: 0670590101; PI: Hui). **E**uropean

Photon **I**maging **C**amera (EPIC) was used throughout this investigation. The PN CCD was operated in small-window mode with a medium filter to block optical stray light. All the events recorded by PN camera are time-tagged with a temporal resolution of 5.7 ms, which enable us to examine the spectral properties at different rotational phases for the first time. On the other hand, the MOS1/2 CCDs were operated in full-window mode with a medium filter in each camera, which provide us with a large field-of-view (15' in radius) for a deep search of X-ray point sources as well as the diffuse X-ray emission from SNR G78.2+2.1. The median satellite boresight pointing during this observation is RA=$20^{\rm h}21^{\rm m}30.56^{\rm s}$ Dec=$+40^{\circ}26^{'}46.8^{''}$ (J2000), which is the position of 2XMM J202131.0+402645 determined by Trepl et al. (2010).

With the most updated instrumental calibration, we generated the event lists from the raw data obtained from all EPIC instruments with the tasks *emproc* and *epproc* of the **XMM**-Newton **S**cience **A**nalysis **S**oftware (XMMSAS version 12.0.1). The event files were subsequently filtered for the energy range from 0.5 keV to 10 keV for all EPIC instruments and selected only those events for which the pattern was between $0-12$ for MOS cameras and $0-4$ for the PN camera. We further cleaned the data by accepting only the good times when the sky background was low and removed all events potentially contaminated by bad pixels. After the filtering, the effective exposures are found to be 85 ks, 72 ks and 77 ks for MOS1, MOS2, PN respectively.

We have also re-analysed the archival *Chandra* data with PSR J2021+4026 on-axis (Obs. ID: 11235, PI: Weisskopf) in order to constrain the evidence for the pulsar wind nebula (PWN). This observation has used the Advanced CCD Imaging Spectrometer (ACIS) with the aim-point on the back-illuminated CCD ACIS-S3 for an exposure of 56 ks. The major results of this observation have already been reported by Weisskopf et al. (2011). In our investigation, we focus on searching for the possible extended emission associated

wtih PSR J2021+4026 with the sub-arcsecond angular resolution of this data, which has not yet been fully explored by Weisskopf et al. (2011). By using the script *chandra_repro* provided in the **C**handra **I**nteractive **A**nalysis **O**bservation software (CIAO 4.3), we have reprocessed the data with CALDB (ver. 4.4.5). Since we aim for a high spatial resolution analysis, sub-pixel event repositioning has been applied during the data reprocessing in order to improve the positional accuracy of each event (cf. Li et al. 2004). We restricted the analysis of this ACIS data in an energy range of $0.3 - 8$ keV.

2.2. Spatial Analysis

The X-ray color images as obtained by MOS1/2 and PN are shown in Figure 1 and Figure 2 respectively (Red:0.5-1 keV; Green:1-2 keV; Blue:2-10 keV). In order to correct for the non-uniformity across the detector and the mirror vignetting, each image has been normalized by the exposure map generated by using the XMMSAS task *eexpmap* for the corresponding detector. The exposure-corrected images have been adaptively smoothed so as to attain a minimum signal-to-noise ratio of 3. This deep observation allows us to search for new X-ray point sources in this field. In Figure 1, point sources with various X-ray hardness can be seen. For determining their positions and count rates, we performed a source detection by using maximum likelihood fitting on MOS1, MOS2 and PN data individually with the aid of the XMMSAS task *edetect_chain*. We set the detection threshold to be 4σ.

By visual inspection, we removed the weak sources which are potentially false detections from the source lists resulted from individual cameras. These include several sources close to the edge of the field-of-view (1 from MOS1, 1 from MOS2, 2 from PN) as well as a few slightly extended sources coincide with the diffuse emission which are likely to be clumps of the supernova remnant (3 from MOS1 and 2 from MOS2). The screened

lists are subsequently correlated and merged by using the XMMSAS task *srcmatch*. In case the position of a source obtained from two detections are consistent within their 3σ uncertainties, they are merged as a single entry. Their source properties are summarized in Table 1[6] Including PSR J2021+4026 (i.e. source 18), 42 distinct point sources are detected within the 30' field-of-view (FoV) around the aim-point in this observation. Among all these X-ray point-like objects in this field, source 8 (XMM J202154.7+402855) is the brightest. A further analysis found that its X-ray flux is significantly variable which worth a deeper investigation. The spectral and temporal analysis of XMM J202154.7+402855 are reported in appendix.

Besides the point source population, faint diffuse X-ray structures have also been seen in this observation. At the southeastern edge of the MOS1/2 image (Fig. 1), extended soft emission is highlighted by the elliptical region. This region partially covers the structure R1 examined by Uchiyama et al. (2002). In the central region, an extended structure around PSR J2021+4026 can be seen in both Fig. 1 and Fig 2. A close-up look of this feature as seen by the PN camera is shown in Figure 2. The solid-line ellipses in Fig. 1 and Figure 2 illustrate the source regions for extracting the spectra from the southeastern and the central parts of G78.2+2.1 respectively (see §2.4).

Apart from reporting the discovery of X-ray pulsation, Lin et al. (2013) have also found that the phase-averaged spectrum can be described by a blackbody plus power-law model. One possible origin for the power-law component is the PWN. Although this *XMM-Newton* observation provides a superior photon statistics for spectral and timing

[6]Table 1 is slightly different from the standard source list given by *XAssist* in three aspects: (1) Multiple detections with positional coincidence are combined as single entry. (2) Potentially false detections are removed by visual inspection. (3) All the tabulated sources have signal-to-noise ratio >4.

analysis, its relatively wide point spread function (PSF) does not allow us to search for the possible compact PWN around the pulsar.

In investigating the *Chandra* ACIS image, Weisskopf et al. (2011) have briefly mentioned a possible feature associated with PSR J2021+4026 which may be indicative of a PWN. By fitting the X-ray image of PSR J2021+4026 with a circular Gaussian plus a constant background, the authors concluded that it is consistent with being point-like and placed an upper-limit of its extent to be $\lesssim 6$". Although this may be useful in quantifying the extent of bright and symmetric nebula (e.g. plerionic emission associated with young pulsars like Crab), such method can overlook faint asymmetric extended feature. This motivates us to reexamine this archival data to characterize the properties of this feature in details. The adaptively-smoothed ACIS image of a $0.5' \times 0.5'$ field around PSR J2021+4026 is shown in Figure 3. It clearly shows a nebula-like structure which extends to west from PSR J2021+4026. For the PWN associated with a fast-moving pulsar, the extended X-ray emission is typically aligned with the direction of proper motion (cf. Gaensler 2005). Although the proper motion of PSR J2021+4026 is unknown, the orientation of its associated extended X-ray PWN indicates that it might be moving eastward. Assuming the birth place of PSR J2021+4026 is not far away from the nominal center of G78.2+2.1 given by Green (2009) (i.e. the white cross in Fig. 1), we speculate the direction of the proper motion by extrapolating from the nominal remnant center to the current pulsar position. The speculated direction is illustrated by the white arrow in Figure 3. It is interesting to notice that it deviates from the symmetric axis of the nebula by only $\sim 5°$.

For quantifying the extent of such elongated compact nebula, we computed its brightness profile along its orientation (Hui et al. 2007, 2008, 2012). We estimated the counts in 18 consecutive boxes with a size of $1'' \times 10''$ from the raw image with a pixel size of $0.5" \times 0.5"$ along the extended feature (see the inset of Fig. 4). The observed brightness

profile is shown in Figure 4. To estimate the background level, we have sampled the source-free regions around PSR J2021+4026 within a $2' \times 2'$ field-of-view. The average background level and its 1σ uncertainties are indicated by the horizontal solid line and dotted lines respectively. The nebular feature apparently extends for $\sim 10''$ to the west before it falls to the estimated background level, which clearly exceeds the upper-limit placed by Weisskopf et al. (2011) through a symmetric Gaussian fitting.

To further examine its emission nature, we have extracted the photons from this feature within a box of $9' \times 6'$ centered at RA=$20^{\rm h}21^{\rm m}30.19^{\rm s}$ Dec=$+40°26'45.2''$ (J2000). Only 25 counts are collected from this observation which forbids any meaningful spectral analysis. However, we can still estimate its X-ray color and compare with PSR J2021+4026. Following Trepl et al. (2010) and Weisskopf et al. (2011), we divide the energy range into three bands: soft (S: 0.5-1 keV), medium (M: 1-2 keV) and hard (H: 2-8 keV). The X-ray colors of this extended feature are estimated to be $(H-S)/T = 0.41 \pm 0.21$ and $M/T = 0.59 \pm 0.16$. In comparison with the X-ray colors of PSR J2021+4026, $(H-S)/T = 0.02 \pm 0.03$ and $M/T = 0.75 \pm 0.02$ (Weisskopf et al. 2011), the X-ray emission from the extended feature is apparently harder which possibly indicates its non-thermal nature.

2.3. Analysis of the pulsed X-ray emission from PSR J2021+4026

2.3.1. Pulsed spectrum of PSR J2021+4026

From the phase-averaged spectral analysis, it has been shown that a single component model is not able to describe the observed data beyond ~ 3 keV (Weisskopf et al. 2011; Lin et al. 2013). Statistically, an additional hard component is required at a confidence level $> 99.995\%$. A blackbody (BB) plus power-law (PL) model fits the data reasonably

well (cf. Fig. 3 in Lin et al. 2013). Although the PWN as seen by *Chandra* is likely to contribute at least a part of this hard component, one cannot rule out the possiblity that the observed non-thermal X-rays are originated from the pulsar magnetosphere and thus have contributions to the observed pulsation. To distinguish these two scenarios, one has to determine in which rotational phases does this PL component dominate. This motivates us to examine the pulsed spectrum of PSR J2021+4026 with the PN data.

We extracted the source spectrum in a circular region of a 20″ radius centered at the X-ray position of PSR J2021+4026 as determined by the source detection algorithm. The adopted extraction region corresponds to an encircled energy function of $\sim 76\%$. For determining the pulse phase of each photon, their arrival times were firstly corrected to the solar system barycenter with the aid of XMMSAS task *barycen* by using the JPL DE405 earth ephemeris. For assigning the pulse phase to each event, we adopted the temporal parameters as determined by Lin et al. (2013).

We divided the rotational phases into two regimes, which are illustrated by the shaded regions in Figure 5. The phase intervals $0.2-0.7$ and $0.85-1.2$ are defined as the "on-pulse" and "off-pulse" components respectively. Assuming the off-pulse component contributes a steady DC level across the entire rotational phase, the pulsed spectrum was then obtained by subtracting the off-pulse component from the on-pulse component. The response files were produced by the XMMSAS task *rmfgen* and *arfgen*. The spectrum is binned so as to have > 50 counts per spectral bin. We used XSPEC 12.7.0 for all the spectral analysis reported in this work. The spectral fits were performed in 0.5-10 keV.

The pulsed spectrum is found to be softer than the phase-averaged spectrum. Majority of the pulsed X-rays have energies < 3 keV (see Figure 6). At energies > 3 keV, $\gtrsim 72\%$ of the collected photons are contributed by the off-pulse component. We further found that the pulsed spectrum can be well described by a simple absorbed blackbody model

($\chi^2 = 12.86$ for 15 D.O.F.) without requiring additional components. The best-fit model yields a column density of $N_{\rm H} = (9.1^{+5.2}_{-3.5}) \times 10^{21}$ cm^{-2}, a temperature of $kT = 0.23^{+0.06}_{-0.05}$ keV, a blackbody emitting region with a radius of $R = 500^{+1053}_{-282} d_2$ m, where d_2 represents the distance to PSR J2021+4026 in unit of 2 kpc. As the uncertainty of $N_{\rm H}$ is large, we fixed it at the value derived from the phase-averaged analysis (Lin et al. 2013), $N_{\rm H} = 7 \times 10^{21}$ cm^{-2}, and constrained the blackbody temperature and radius to be $kT = 0.26^{+0.03}_{-0.02}$ keV and $R = 318^{+101}_{-77} d_2$ m respectively ($\chi^2 = 13.51$ for 16 D.O.F.). For a conservative estimate, all the quoted errors of the spectral parameters are 1σ for two parameters of interest (i.e. $\Delta\chi^2 = 2.30$ above the minimum).

We have also attempted to perform a phase-resolved spectroscopy for each phase bin in Figure 5 in order to investigate how does the spectral properties varies across the rotational phase. However, the photon statistic for individual phase bins is generally too small for a constraining analysis. The high instrumental background has further exacerbated the situation. Therefore, such analysis will not be further considered for this observation.

2.3.2. Multi-epoch X-ray spectral analysis of PSR J2021+4026.

As mentioned in the introduction, PSR J2021+4026 is the first variable radio-quiet $\gamma-$ray pulsar where its $\gamma-$ray flux as spin-down properties suddenly change around MJD 55850 (2011 October 16). Allafort et al. (2013) argued that the variability of the $\gamma-$ray pulsed emission is due to certain global change in the magnetosphere. Since the X-ray emission from the hot polar cap is resulted from the bombardment of the backflow current from the outergap (Cheng & Zhang 1999), it is not unreasonable to speculate that the change in the $\gamma-$ray properties might be accompanied with the change in X-ray.

In the context of the outergap model (Cheng & Zhang 1999), the γ-ray luminosity is

given by $L_\gamma \sim f^3 \dot{E}$ where f is the fractional size of the outergap. Therefore, the observed change in the γ-ray luminosity, $\delta L_\gamma / L_\gamma \sim 18\%$ (Allafort et al. 2013), implies the gap size changed by $\delta f/f \sim \delta L_\gamma / 3L_\gamma \sim 6\%$. Since our analysis suggests the pulsed X-ray emission is thermal, this can be produced through the polar cap heating by the return particle flux $\dot{N_p} = f\dot{N_{\rm GJ}}$ where $\dot{N_{\rm GJ}}$ is the Goldreich-Julian particle flux (Goldreich & Julian 1969). The X-ray luminosity can thus be estimated by $L_X \sim \dot{N}_p E_p$ where E_p is the typical particle energy deposited on the stellar surface. Therefore, the expected change in L_X is found to be $\delta L_X / L_X \sim \delta \dot{N}_p / \dot{N}_p \sim \delta f/f \sim 6\%$.

Since the *Chandra* (MJD 55435) and the *XMM-Newton* (MJD 56028) observations used in this study were performed before and after $\gamma-$ray flux jump, it is instructive to examine if PSR J2021+4026 exhibited any X-ray variability. In order to investigate whether the X-ray spectral properties of PSR J2021+4026 vary, we examined the phase-averaged spectra of PSR J2021+4026 as obtained by *Chandra* ACIS-S3 and all EPIC camera on *XMM-Newton*. For *Chandra*, we extracted the source spectrum from a circular region with a radius of 2" centered at the pulsar position. The background spectrum was sampled from an annular region with inner/outer radii of 2.5"/4" around the pulsar. For *XMM-Newton*, we followed the same procedure adopted by Lin et al. (2013) in preparing the phase-averaged spectrum.

We jointly fitted an absorbed BB+PL model to the *Chandra* and *XMM-Newton* spectra with the column absorption tied together throughout the analysis. In order to minimize the number of free parameters, we examined the variability of each spectral component one at a time. First, with the PL component in different epoch tied together, we allowed the BB component of the spectrum in different epoch to vary independently during the fitting. This yielded a column absorption of $N_H = 6.4^{+0.8}_{-1.8} \times 10^{21}$ cm^{-2}, a photon index of $\Gamma = 1.5 \pm 0.8$ and a PL normalization of $3.6^{+6.8}_{-2.6} \times 10^{-6}$ photons keV^{-1} cm^{-2} s^{-1} at 1 keV. For the BB component, the best-fit temperature and emission radius for the epoch

MJD 55435 are $kT = 0.22 \pm 0.04$ keV and $R = 350^{+359}_{-94} d_2$ m respectively. After the $\gamma-$ray flux change, the BB parameters are found to be $kT = 0.24^{+0.04}_{-0.02}$ keV and $R = 288^{+193}_{-27} d_2$ m in the epoch MJD 56028.

For inspecting the possible variability of the PL component, the BB components of both spectra were tied. It yielded a column absorption of $N_H = 6.4^{+0.8}_{-1.8} \times 10^{21}$ cm^{-2}, a blackbody temperature of $kT = 0.24 \pm 0.04$ keV and a emission radius of $R = 298^{+22}_{-96} d_2$ m. The photon index and PL normalization before the $\gamma-$ray flux change are found to be $\Gamma = 1.0^{+2.0}_{-1.0}$ and $1.4^{+11.1}_{-1.4} \times 10^{-6}$ photons keV^{-1} cm^{-2} s^{-1} at 1 keV. The corresponding parameters after the $\gamma-$ray flux change are $\Gamma = 1.8 \pm 0.8$ and $5.4^{+10.1}_{-3.7} \times 10^{-6}$ photons keV^{-1} cm^{-2} s^{-1} at 1 keV.

Within the tolerence of the quoted statistical uncertainties, neither the pulsed thermal X-ray component nor the unpulsed non-thermal X-ray component are found to be variable in these two epochs.

2.3.3. Analysis of the X-ray pulse profile of PSR J2021+4026.

The X-ray pulse profile can also be used to investigate the global properties of the neutron star. As the polar cap sweeps across our line-of-sight, modulation in soft X-ray regime can be seen (cf. Hui & Cheng 2004; Pechenick et al. 1983). Since the gravity of a neutron star is tremendous, the shape of thermal X-ray pulse profile is determined by the near-field spacetime curvature. The effect of gravity on the trajectory of emitted photons, which depends on the mass-to-radius ratio of the neutron star, must be considered in modeling the light curve.

Following Pechenick et al. (1983), we simulated the X-ray pulse profile resulted from the general relativistic calculation and compare with the observational result. We choose our coordinates so that the observer is on the positive z-axis at $r = r_0$ where $r_0 \to \infty$

(cf. Fig. 6 in Hui & Cheng 2004). We described the stellar surface by angular spherical coordinates θ and ϕ where θ is measured from the z-axis defined above. For the photon emitted at an angle δ from the stellar surface, it will seem to the observer that they are emitted at an angle $\theta^{'}$ from the z-axis as a result of gravitational light bending. The relationship between θ and $\theta^{'}$ is given by:

$$\theta = \int_0^{\frac{GM}{Rc^2}} \left[\left(\frac{GM}{bc^2} \right)^2 - (1-2u)\, u^2 \right]^{-1/2} du, \tag{1}$$

where $b = r_0 \theta^{'}$ is the impact parameter of the photon and $u = GM/c^2 r$.

For a neutron star, $\frac{GM}{c^2 R}$ must be less than 1/3. Therefore, a photon emitted from the surface that reaches the observer must have an impact parameter $b \leq b_{max}$ where $b_{max} = R\,(1 - 2GM/c^2 R)^{-1/2}$ (Pechenick et al. 1983). The condition $b = b_{max}$ sets the maximum value of θ, namely θ_{max}.

Considering a polar cap of an angular radius of α centered at $\theta = \theta_0$, a function $h(\theta; \alpha, \theta_0)$ is then defined as the range of ϕ included in the "one-dimensional slice" at θ of the polar cap (cf. Fig. 6 in Hui & Cheng 2004). If $\theta_0 + \alpha \leq \theta_{max} \leq 180^o$ and $\theta_0 - \alpha \geq 0$, then $h(\theta; \alpha, \theta_0)$ is defined as:

$$h(\theta; \alpha, \theta_0) = \begin{cases} 2\cos^{-1}\left(\frac{\cos\alpha - \cos\theta_0 \cos\theta}{\sin\theta_0 \sin\theta} \right) & \text{for } \theta_0 - \alpha \leq \theta \leq \theta_0 + \alpha; \\ 0 & \text{for } \theta \text{ outside the range } \theta_0 \pm \alpha \end{cases} \tag{2}$$

For generating the light curves, θ_0 is expressed as a function of time/rotational phase. Let β is the angle between the axis of rotation of the star and the line joining the center of the polar cap and the center of the star, and γ is the angle between the axis of rotation and the z-axis, then

$$\cos\theta_0 = \sin(\beta)\sin(\gamma)\cos(\Omega t) + \cos(\beta)\cos(\gamma) \tag{3}$$

where Ω is the rotational frequency of the star. The relative brightness can be expressed as a function θ_0, M/R and α:

$$A\left(\theta_0; M/R, \alpha\right) = \left(1 - \frac{2GM}{c^2R}\right)^2 \left(\frac{GM}{c^2R}\right)^2 \int_0^{x_{max}} h\left(x; \alpha, \theta_0\right) x\, dx \tag{4}$$

where $x = \frac{c^2 b}{GM}$ and $x_{max} = \frac{c^2 b_{max}}{GM}$.

With a view to minimize the number of free parameters in the modeling, we utilized the results from other analysis. From the best-fit BB model of pulsed spectrum, the polar cap size is found to be ~ 320 m if PSR J2021+4026 locates at a distance of 2 kpc. Assuming a neutron star radius of $R \sim 10$ km, we fixed the angular radius of the polar cap at $\alpha \sim 2^\circ$. From modeling the γ-ray light curve, Trepl et al. (2010) suggest the viewing angle can possibly be in a range of 83-87°. For a given mass-to-radius ratio, $\frac{GM}{c^2R}$, the effect of varying the viewing angle in such small range in the pulse profile is negligible. Also, for a polar cap with a small angular radius of $\sim 2^\circ$, it is likely that only one pole will cross the line-of-sight. This scenario is supported by the observed single broad peak. With these constraints, we minimized the number of free parameters by assuming a simple orthogonal rotator ($\gamma = \beta = 90^\circ$) with a single pole contribution. This leaves the $\frac{GM}{c^2R}$ to be the only parameter for modeling the X-ray light curve. The best-fit model yields $\frac{GM}{c^2R} = 0.21$ and a goodness-of-fit of $\chi^2 = 27.1$ for 31 D.O.F.. For $R \sim 10$ km, it implies a neutron star mass of $M \sim 1.4 M_\odot$. The comparison of the best-fit model and the observed light curve is shown in Figure 7. For a conservative estimate, the 90% confidence interval for 1 parameter of interest (i.e. $\Delta\chi^2 = 2.71$ above the minimum) is found to be $0.17 < \frac{GM}{c^2R} < 0.25$, which corresponds to $M \sim 1.2 - 1.7 M_\odot$ for $R \sim 10$ km. Analysis with deeper follow-up observation can provide a tighter constraint on the mass-to-radius ratio of this neutron star.

2.4. Imaging spectroscopy of the central and southeastern regions of G78.2+2.1

For investigating the X-ray emission from G78.2+2.1, we only focused on the extended features with relatively high surface brightness which are highlighted by the solid-line ellipses in Fig. 1 (referred as southeastern region hereafter) and Fig. 2 (referred as central region hereafter). Before the spectra of these extended structures were extracted, contributions from all the resolved point sources were firstly subtracted from the data. The background spectra for the southeastern region and the central region were sampled from the nearby low count regions as illustrated by the dash-ellipse in Fig 1 and dash-circle in Fig. 2 respectively. The response files for this extended source analysis are generated by *rmfgen* and *arfgen* with uniform spatial averaging. The spectra obtained from different cameras were binned dynamically so as to achieve a comparable signal-to-noise ratio.

By inspecting the X-ray spectrum of the central region (see Fig. 8), some emission line features such as Mg at $\sim$ 1.4 keV and Si at $\sim$ 1.9 keV can be clearly seen. This prompts us to examine the spectrum with an absorbed collision ionization equilibrium (CIE) plasma model (XSPEC model: VEQUIL). To examine whether the metal abundance of G78.2+2.1 deviates from the solar values, we thawed the corresponding parameters individually to see if the goodness of fit can be improved. The best-fit model yields a plasma temperature of $kT \sim 0.6$ keV and a column absorption of $N_H \sim 10^{22}$ cm^{-2}. There is also indication that Mg is overabundant in comparison with the solar values. However, such model cannot provide an adequate description of the observed data even with metal abundance Mg open as free parameter ($\chi^2 = 391.53$ for 159 D.O.F.). By examining the fitting residuals, systematic deviations at energies beyond $\sim$ 2 keV are noted. We suspected that an extra PL component might be required. With the additional PL component, the goodness-of-fit has been significantly improved ($\chi^2 = 209.36$ for 157

D.O.F.). It yields a column absorption of $N_H = 8.2^{+0.8}_{-1.0} \times 10^{21}$ cm^{-2}, a plasma temperature of $kT = 0.59^{+0.02}_{-0.03}$ keV, a Mg abundance of $1.9^{+0.4}_{-0.3}$ with respect to the solar value, a emission measure of $\int_V n_e n_H dV = (2.8 \pm 0.9) \times 10^{11} D^2$ cm^{-3} and a PL index of $\Gamma = 1.6^{+0.5}_{-0.2}$, where n_e, n_H, V and D are the electron density (cm^{-3}), hydrogen density (cm^{-3}), volume of interest (cm^3) and the source distance (cm).

For further improving the spectral modeling, we examined the fitting residuals of the CIE+PL fit. We noticed there are scattering of the residuals at energies greater than ~ 2 keV which are probably stemmed from the additonal PL. As demonstrated by Huang et al. (2014), the residuals in the hard band can possibly resulted from the residual soft proton contamination in individual cameras after the data screening. And therefore, instead of originating from the particle acceleration, the additional PL component merely provides a phenomenological description for such residual soft proton background with the PL index and normalization vary among different EPIC cameras. By disentangling the PL component in MOS1, MOS2 and PN, we found the goodness-of-fit can be further improved ($\chi^2 = 175.04$ for 153 D.O.F.). In view of the different best-fit PL index inferred from different cameras, we conclude that the residuals in the hard band are contributed by the residual background. Under this consideration, the best-fit absorbed CIE component yields $N_H = 7.9^{+0.8}_{-0.5} \times 10^{21}$ cm^{-2}, $kT = 0.60^{+0.02}_{-0.03}$ keV, a Mg abundance of 2.0 ± 0.4 with respect to the solar value and $\int_V n_e n_H dV = 2.5^{+0.8}_{-0.5} \times 10^{11} D^2$ cm^{-3}.

We have also examined the central part of G78.2+2.1 with an non-equilibrium ionization (NEI) model (XSPEC model: VNEI). With additional PL component applied to account for the residual soft proton contamination in the individual camera, we found that the NEI model results in a further improved goodness-of-fit ($\chi^2 = 167.95$ for 152 D.O.F.). It yields a column absorption of $N_H = 7.4^{+1.0}_{-1.4} \times 10^{21}$ cm^{-2}, a plasma temperature of $kT = 1.6^{+0.6}_{-0.3}$ keV, a Mg abundance of 1.6 ± 0.2 with respect to the solar value, a

emission measure of $\int_V n_e n_H dV = 7.4^{+1.0}_{-0.8} \times 10^{10} D^2$ cm^{-3} and an ionization timescale of $n_e t = 1.8^{+0.6}_{-0.4} \times 10^{10}$ s cm^{-3} where n_e and t are electron density and time elapsed since the gas has been shock-heated respectively. We noted that the inferred plasma temperature is significantly higher than the CIE fit. This can be due to the effect that the ionization states for a plasma in NEI at a given temperature are lower than those in the CIE situation (e.g. see Fig. 11 in Vink 2012). Assuming a CIE condition can thus result in an underestimation of the plasma temperature. The NEI condition is further indicated by the best-fitted ionization timescale which is significantly less than that ($n_e t \sim 10^{12}$ s cm^{-3}) required to reach CIE (cf. Vink 2012). In view of these, the NEI scenario is preferred.

For fitting the spectrum in the southeastern region, we have also considered both CIE and NEI models. Same as the situation in the analysis of the diffuse X-rays from the central region, additional PL component were included for modeling the residual soft proton contamination in MOS1 and MOS2 individually. The CIE yields $N_H = 4.4^{+1.0}_{-0.7} \times 10^{21}$ cm^{-2}, $kT = 0.63^{+0.02}_{-0.03}$ keV, a Mg abundance of 3.3 ± 0.8 with respect to the solar value and $\int_V n_e n_H dV = 5.1^{+2.5}_{-1.1} \times 10^{11} D^2$ cm^{-3} ($\chi^2 = 305.11$ for 242 D.O.F.). In comparison, the NEI model results in an improved goodness-of-fit ($\chi^2 = 261.06$ for 241 D.O.F.). It yields $N_H = (7.4 \pm 0.6) \times 10^{21}$ cm^{-2}, $kT = 1.1^{+0.5}_{-0.3}$ keV, a Mg abundance of 1.2 ± 0.1 with respect to the solar value, $\tau = n_e t = 2.4^{+1.9}_{-0.7} \times 10^{10}$ s cm^{-3} and $\int_V n_e n_H dV = 8.2^{+3.4}_{-1.9} \times 10^{11} D^2$ cm^{-3}. Both the goodness-of-fit and the small value of $n_e t$ resulted from this fit suggest the remnant emission in this region is also in an NEI condition.

3. DISCUSSION

We have reported the results from a detailed X-ray analysis of PSR J2021+4026 and G78.2+2.1. The column absorption deduced from the X-ray spectra of PSR J2021+4026 (see §2.3) is consistent with that deduced from various parts of the diffuse emission (§2.4).

And we note that it is also consistent with neutral hydrogen density inferred from the HI absorption spectrum (Leahy et al. 2013). These indicate that the pulsar emission, diffuse X-ray emission and the radio shell are essentially at the same distance. Hence, the association between PSR J2021+4026 and G78.2+2.1 is supported by our investigation.

Given the pulsar-SNR association and assuming the birth place of PSR J2021+4026 is not far away from the geometrical center of G78.2+2.1, we estimated the projected velocity of the pulsar. The angular separation between PSR J2021+4026 and the geometrical center is $\sim 0.1^{\circ}$ (cf. Fig. 1). At a distance of 2 kpc, this corresponds to a physical separation of 1.4×10^{14} km. Together with a Sedov age of ~ 8000 yrs deduced for G78.2+2.1 (Leahy et al. 2013), the magnitude of the projected velocity of PSR J2021+4026 is expected to be $v_p \sim 550$ km s^{-1} which is not unreasonable for the known pulsar population (Hobbs et al. 2005). The projected direction of the pulsar motion is indicated by the arrow in Fig. 3. The speculated pulsar motion can possibly be checked by a dedicated $\gamma-$ray timing analysis of the full time-span *Fermi* LAT data in further studies.

Such speculated pulsar velocity should be far exceeding the local speed of sound. For a pulsar moving supersonically, it is expected to drive a bow shock through the ambient medium. The pulsar wind particles will be accelerated and produce synchrotron X-ray emission. With the motion of pulsar, this will result in a cometary-like nebula as the extended structure found in the high resolution *Chandra* image (see Fig. 3 and Fig. 4). In this case, the termination shock radius R_s is determined by the ram pressure balance between the relativistic pulsar wind particles and the circumstellar medium at the head of the shock:

$$R_s \simeq \left(\frac{\dot{E}}{2\pi\rho v_p^2 c}\right)^{1/2} \sim 3 \times 10^{16} \dot{E}_{34}^{1/2} n^{-1/2} v_{p,100}^{-1} \mathrm{cm}, \quad (5)$$

where $v_{p,100}$ is the velocity of the pulsar in units of 100 km s^{-1}, $\dot{E}_{34}$ is the spin-down luminosity of the pulsar in units of 10^{34} erg s^{-1}, and n is the number density of the circumstellar medium in units of cm^{-3}.

For constraining n, we utilized the results inferred by the NEI plasma model fit of the central extended X-ray emission of G78.2+2.1 which surrounds PSR J2021+4026 (see Fig. 2). The best-fit emission measure of this feature allows us to estimate the hydrogen density $n_{\rm H}$ and the electron density $n_{\rm e}$ in this circumstellar region. Assuming n_e and n_H are uniform in the extraction region and distance of 2 kpc, the emission measure can be approximated by $n_e n_H V \sim 2.8 \times 10^{54}$ cm^{-3}. We further assumed a geometry of oblated spheroid for the spectral extraction region, the volume of interest is $V \sim 4 \times 10^{55}$ cm^3. For a fully ionized plasma with $\sim 10\%$ He ($n_{\rm e} \sim 1.2 n_{\rm H}$), n_H is estimated as ~ 0.24 cm^{-3}. Together with the spin-down power of $\dot{E}_{34} = 10$ and our speculated $v_{p,100} \sim 5.5$, Equation 5 implies a termination radius of $R_s \sim 3.5 \times 10^{16}$ cm. It corresponds to a stand-off angle of ~ 1" ahead of the pulsar at a distance of 2 kpc. Comparing this estimate to the angular size of the cometary-like feature behind the pulsar (see Fig. 3), the ratio of termination shock radii between the directions immediately behind and directly ahead of the pulsar is estimated to be ~ 10 which is comparable with the ratios observed in other fast-moving pulsar such as PSR J1747-2958 (Gaensler et al. 2004).

At 2 kpc, the physical size of the synchrotron X-ray nebula associated with PSR J2021+4026 is $l_{\rm pwn} \sim 3 \times 10^{17}$ cm. This implies the timescale for the pulsar to traverse its nebula is $\tau_{\rm pwn} = l_{\rm pwn}/v_p \sim 170$ yrs. The magnetic field strength of the nebula can be estimated by assuming $\tau_{\rm pwn}$ is comparable with the synchrotron cooling timescale of the electrons:

$$\tau_{\rm syn} = \frac{6\pi m_e c}{\gamma \sigma_T B^2} \simeq 10^5 \left(\frac{h\nu_X}{\rm keV}\right)^{-\frac{1}{2}} B_{\mu G}^{-\frac{3}{2}} {\rm yrs} \quad (6)$$

where γ is the Lorentz factor of the wind, σ_T is the Thompson cross section, $\nu_X = 3\gamma^2 eB/2m_e c$ is the characteristic synchrotron frequency and $B_{\mu G}$ is the magnetic field in the shocked region in unit of micro gauss. This suggests the nebular magnetic strength is at the order of $\sim 15\ \mu G$ for a characteristic energy of $h\nu_X$ ∼1 keV.

The magnetic field estimate can further enable us to compute the electron synchrotron cooling frequency $\nu_{\rm c}$:

$$\nu_{\rm c} = \frac{18\pi e m_e c}{\sigma_T^2 \tau_{\rm syn}^2 B^3} \tag{7}$$

which is estimated to be $\sim 1.7 \times 10^{19}$ Hz (i.e. $h\nu_{\rm c} \sim 70$ keV). Since this is far exceeding the observed frequencies, it suggests the X-ray emission of the nebula is in a slow cooling regime (Chevalier 2000; Cheng, Taam & Wang 2004). In this regime, electrons with the energy distribution, $N(\gamma) \propto \gamma^{-p}$, are able to radiate their energy in the trail with photon index $\Gamma = (p+1)/2$. The index p due to shock acceleration typically lies between 2 and 3 (cf. Cheng et al. 2004 and reference therein). This would result in a photon index $\sim 1.5 - 2.0$. This is consistent with the observed photon index of $\Gamma \sim 1.5$ for the unpulsed non-thermal spectral component of PSR J2021+4026.

For the X-ray pulsation of PSR J2021+4026, our analysis of the pulsed spectrum confirmed its thermal origin. We noted that the best-fit blackbody radius is comparable with the polar cap size of $\sqrt{\frac{2\pi R}{cP}} \sim 300$ m by adopting a dipolar field geometry, a neutron star radius of R =10 km and a rotational period of $P = 265$ ms. This suggests the thermal emission is originated from the hot polar cap. Such assertion is further demonstrated by the agreement between the X-ray pulse profile and the simulated modulation by a hot spot on the surface of a canonical rotating neutron star (Fig. 7).

The most remarkable properties of PSR J2021+4026 are the sudden changes of its

spin-down rate, pulse profile and flux in $\gamma-$ray on a timescale shorter than a week (Allafort et al. 2013). The authors speculated that such abrupt changes are resulted from a shift in the magnetic field structure which in turn leads to the change of either magnetic inclination and/or the effective current (see discussion in Allafort et al. 2013). These can be precipitated by a reconfiguration of the magnetic field line footprints on the stellar surface. The polar cap size is defined by the footprint of the last open-field lines and its temperature is determined by the backflow current from the accelerating region. Therefore, according to the scenario proposed by Allafort et al. (2013), one should expect a correlated change in the thermal X-ray flux and/or the X-ray pulse profile.

We have attempted to look for such expected X-ray change across the $\gamma-$ray jump by a joint analysis of *Chandra* and *XMM-Newton* data. Although we did not find any conclusive variability, we would like to point out that the significance of the analysis is limited by the small photon statistic of *Chandra* data. Also, the poor temporal resolution of this *Chandra* data does not allow any investigation of the X-ray pulsation. For a follow-up investigation of this unique pulsar, we encourage a long-term coordinated X-ray and $\gamma-$ray monitoring with *XMM-Newton* and *Fermi* which can provide a better understanding the nature of its variability.

Apart from PSR J2021+4026, we have examined the diffuse X-ray emission of G78.2+2.1 in the FoV of our *XMM-Newton* observation (See §2.4). Leahy et al. (2013) have also analysed the central region with *Chandra* data and obtained $N_H = (7.5 - 11.1) \times 10^{21}$ cm^{-2}, $kT = 0.6 - 2.7$ keV and $n_e t = (1.7 - 12) \times 10^{10}$ s cm^{-3}. Within the tolerence of 1σ uncertainties, our results are consistent with theirs. With the much improved photon statistic of our *XMM-Newton* data, we constrained the spectral parameters N_H, kT and $n_e t$ to an accuracy of $\sim 32\%$, $\sim 56\%$ and $\sim 56\%$ respectively. For comparison, the uncertainties of the corresponding parameters reported by Leahy et al. (2013) are $\sim 39\%$, $\sim 203\%$ and

$\sim 312\%$.

For the southeastern rim, Uchiyama et al. (2002) have investigated its X-ray properties with *ASCA* (R2 region in their work). They have modeled the spectrum with a CIE model and obtained a temperature $kT = 0.53 \pm 0.07$ keV which is consistent with our CIE estimate. However, the quality of *ASCA* data did not allow the authors to discern whether the X-ray emission is in CIE or NEI state.

In our study, we confirmed that the remnant emission from our investigated regions are in NEI state. This is probably due to the low electron density and the time elapsed since the gas has been shock-heated is not long enough for the plasma to reach the equilibrium. The best-fit emission measures and the ionization timescales allow us to estimate these quantities. From the above discussion, the electron density of the central region is found to be $n_e \sim 0.3$ cm^{-3}. With the best-fit ionization timescale of $n_e t \sim 1.8 \times 10^{10}$ s cm^{-3}, the elapsed time since the arrival of the shock is estimated as $t \sim 1900$ yrs. For the diffuse emission in the southeastern region, the emission measure and the volume of interest are $n_e n_H V \sim 3.1 \times 10^{55}$ cm^{-3} and $V \sim 10^{57}$ cm^{-3} respectively. This implies a electron density of $n_e \sim 0.2$ cm^{-3} in this region. Together with the ionization timescale of $n_e t \sim 2.4 \times 10^{10}$ s cm^{-3} inferred for this region, this suggests the gas has been shock-heated ~ 3800 yrs ago. Such age estimates are significantly smaller than the Sedov age of G78.2+2.1 (Leahy et al. 2013). This might indicate that these plasma have been heated by the reverse shock(s) that have returned to the remnant center not long ago. We would like to point out this interpretation is stemmed from the spectral fitting with a relatively simple NEI model. For example, the temperatures of different plasma constituents for such small ionization timescale are not neccessary to equilibrate. A more sophisticated modeling of the observed remnant spectrum around the center can help to confirm if the reverse shocks have arrived yet.

CYH is supported by the Chungnam National University research fund in 2014. CPH and YC are supported by the Ministry of Science and Technology through the grant NSC 102-2112-M-008-020-MY3. JT and KSC are supported by a 2014 GRF grant of Hong Kong Government under HKU 17300814P. AKHK is supported by the Ministry of Science and Technology of Taiwan through grants 100-2628-M-007-002-MY3, 100-2923-M-007-001-MY3 and 103-2628-M-007-003-MY3.

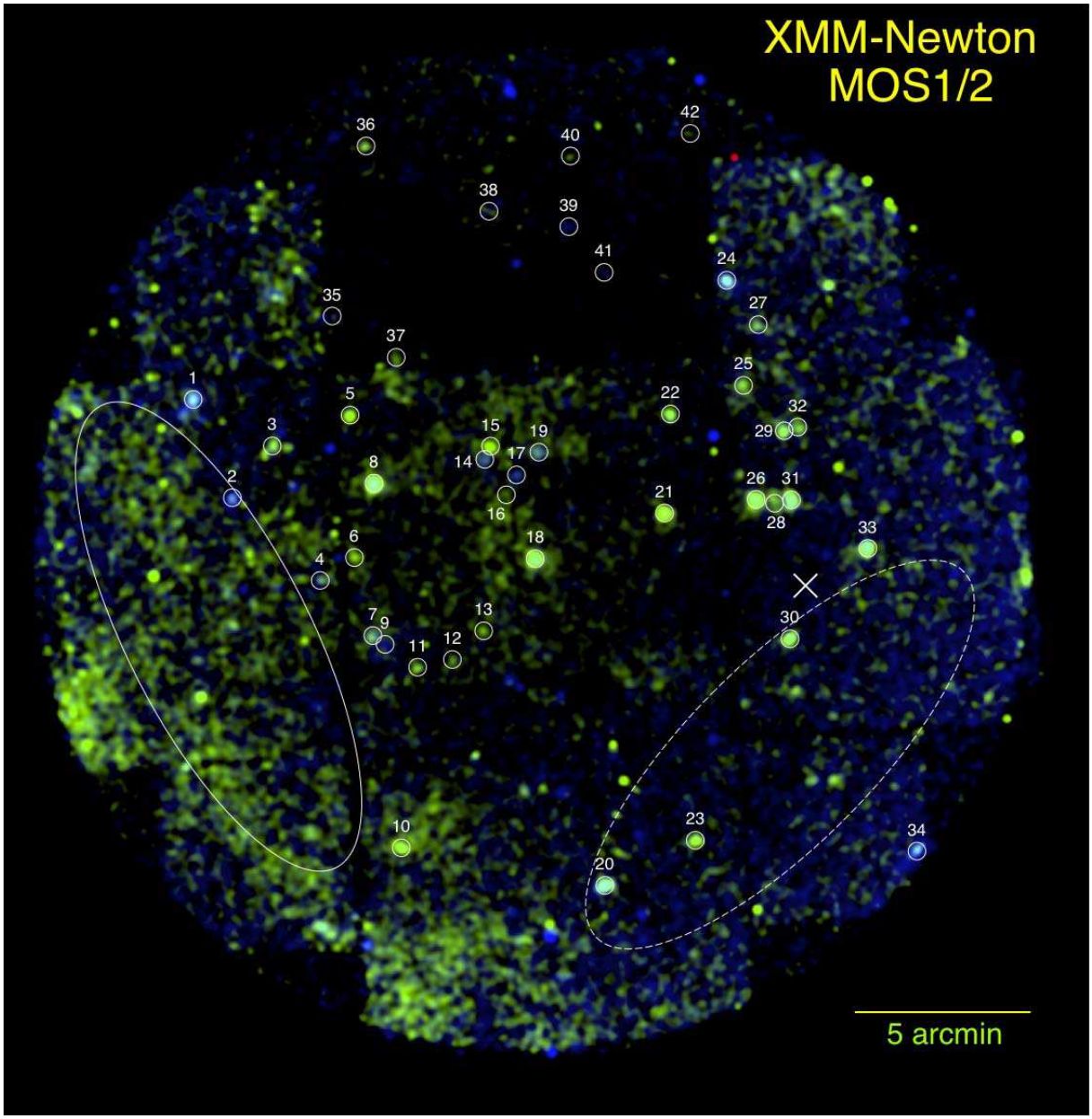

Fig. 1.— Vignetting-corrected *XMM-Newton* MOS1/2 color image of the field around PSR J2021+4026 (red: 0.5-1 keV, green: 1-2 keV, blue: 2-10 keV). The binning factor of this image is 1". Adaptive smoothing has been applied to achieve a minimum signal-to-noise ratio of 3. The white cross illustrates the the nominal geometrical center of SNR G78.2+2.1 (Green 2009). Soft diffuse emission is found in the field. The overlaid solid-line ellipse illustrates the extraction region for the diffuse spectra of the southeastern rim of G78.2+2.1. The dashed ellipse shows the background region used in the remnant analysis. Including PSR J2021+4026 (source 18), 42 X-ray point sources detected by this observation are highlighted with the labels consistent with Table 1. Top is north and left is east.

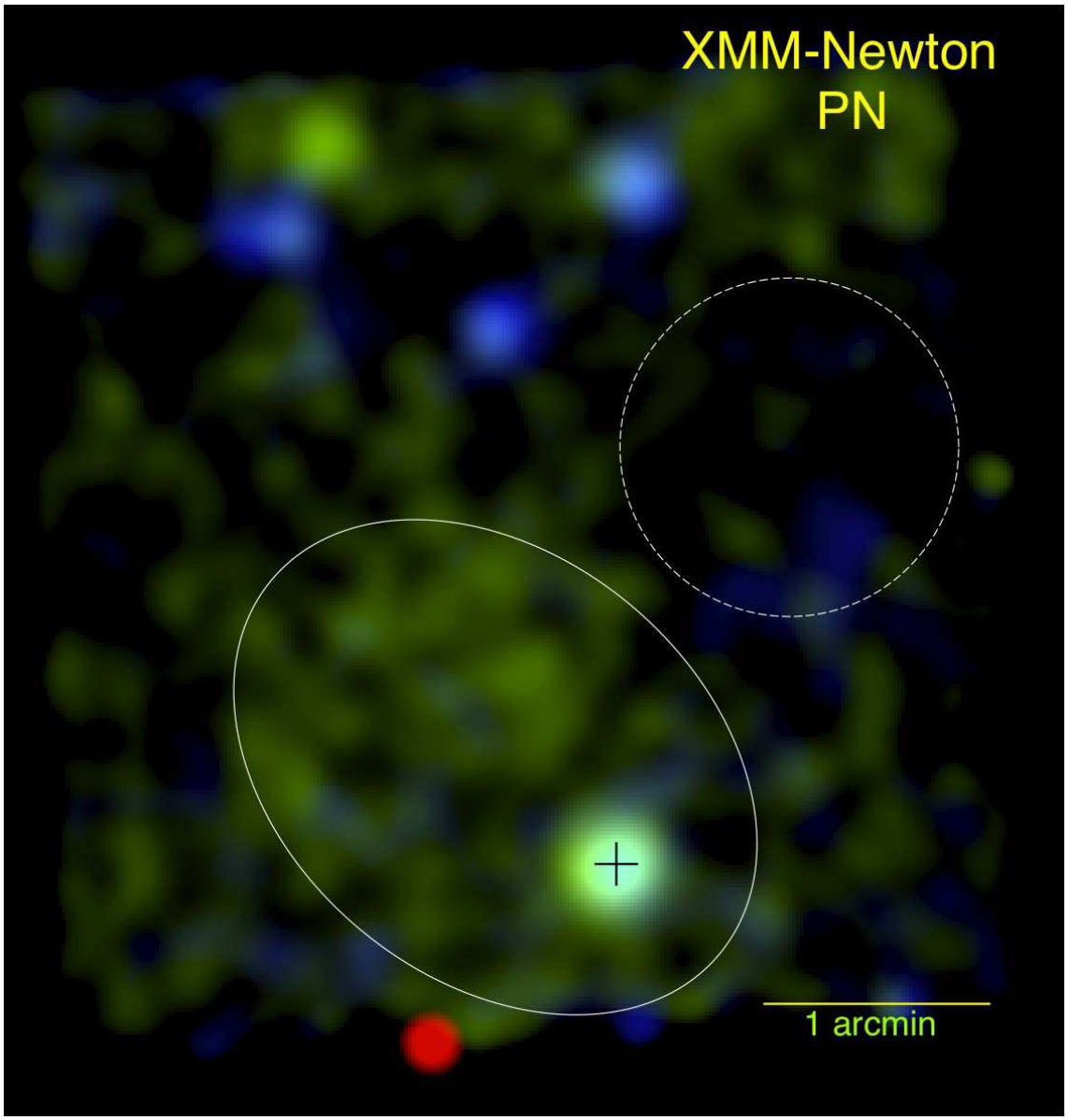

Fig. 2.— The sky region around PSR J2021+4026 (illustrated by the black cross) as seen by *XMM-Newton* PN camera in small-window mode. This image is binned, color-coded, vignetting-corrected and adaptively smoothed in the same way as Fig. 1. Soft emission around the pulsar can be clearly seen. A cocoon-like feature around PSR J2021+4026 is highlighted by a solid-line ellipse which is adopted as the extraction region for the spectra from all EPIC cameras. The dashed circle shows the background region used in the remnant analysis. The bright red spot at the bottom is an artifact at edge of the window. Top is north and left is east.

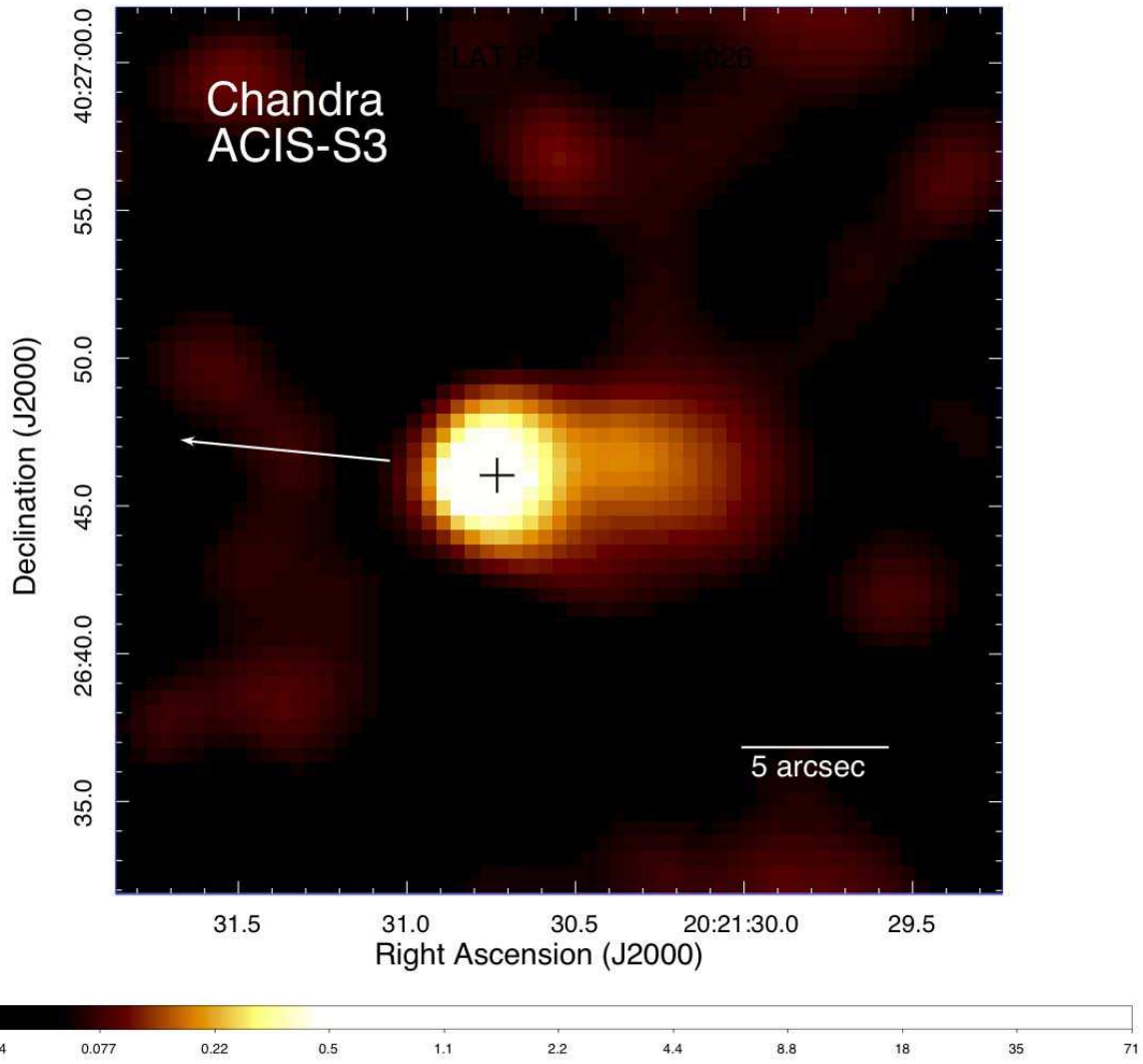

Fig. 3.— The 30" × 30" X-ray image in the energy band 0.3-8 keV around PSR J2021+4026 as seen by *Chandra* ACIS-S3 CCD. The X-ray position as determined by Weisskopf et al. (2011) is illustrated by the black cross. The binning factor of the image is 0.5" and has been adaptively smoothed to achieve a minimum signal-to-noise ratio of 3. A nebular structure extends to the west from the pulsar can be clearly seen. The white arrow illustrates the speculated proper motion direction by extrapolating the nominal center of G78.2+2.1 to the current pulsar position.

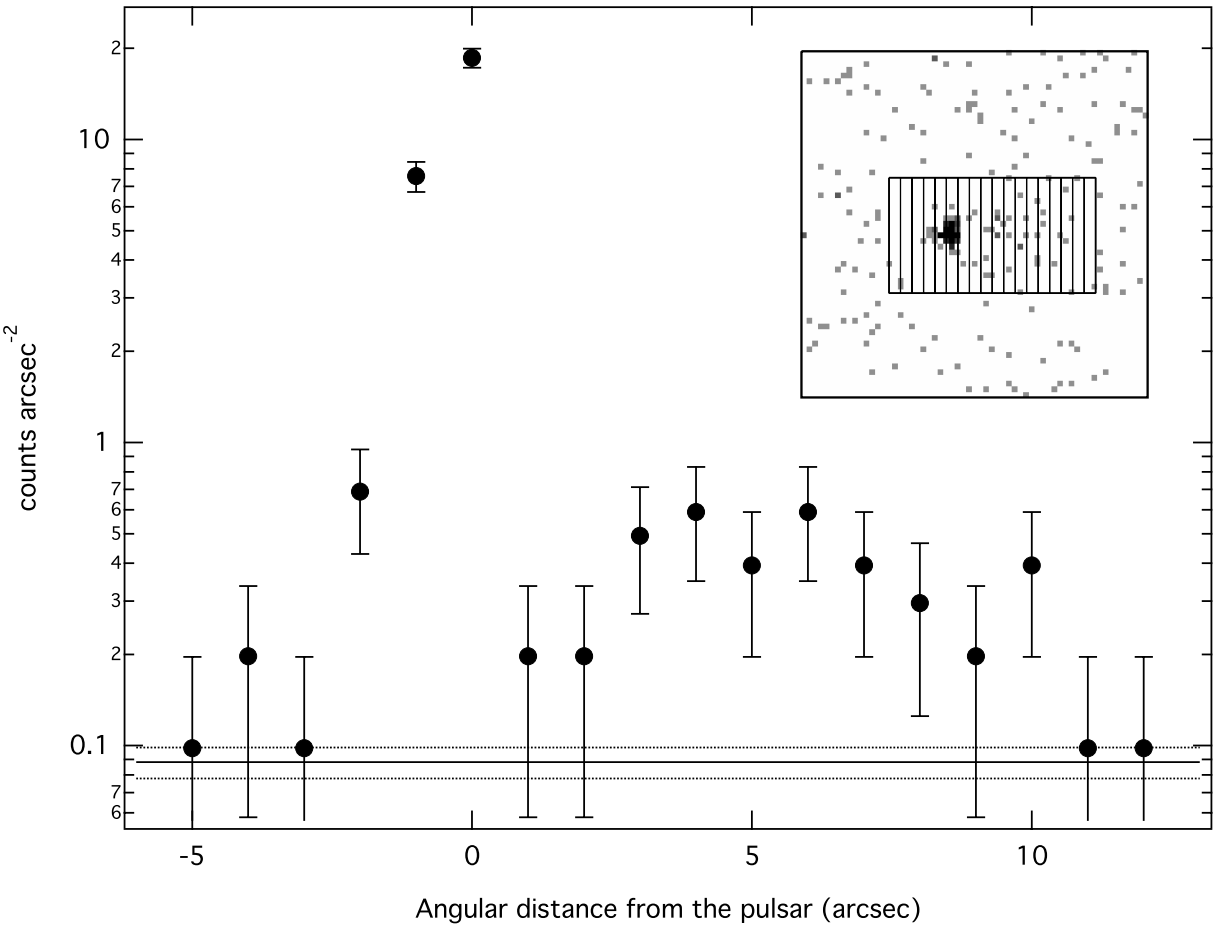

Fig. 4.— The X-ray brightness profile in the energy band of $0.3-8$ keV along the orientation of the PWN associated with PSR J2021+4026 as observed by *Chandra* ACIS-S3 CCD (cf. Fig. 3). The insets show the bins used in computing the profile. Each bin has a size of $1'' \times 10''$. The average background level and its 1σ deviation are indicated by horizontal lines which were calculated by sampling from the source-free regions within a $2' \times 2'$ field around the pulsar.

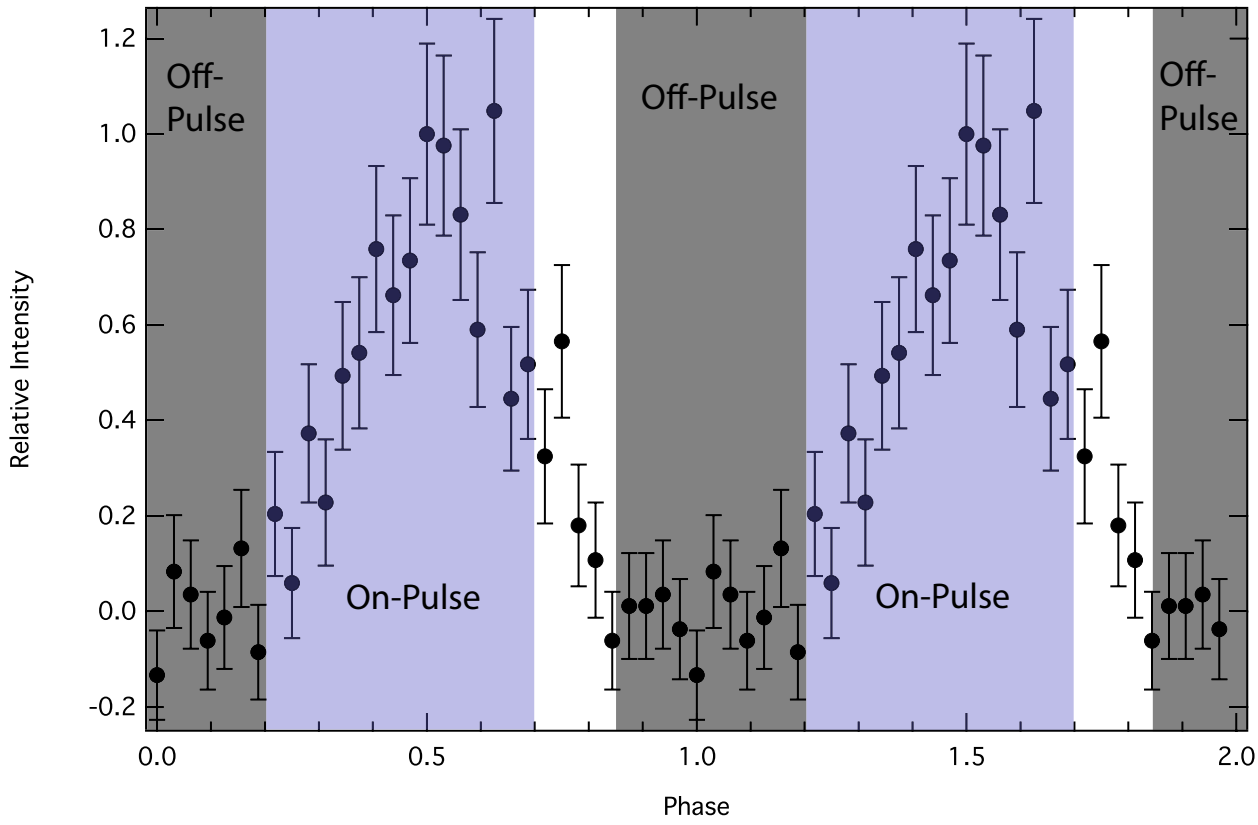

Fig. 5.— The pulsation and quiescent stage labelled by the pulse profile of PSR J2021+4026 (0.7-2 keV) as observed by *XMM-Newton*/PN camera. The obtained light curve was folded with a spin frequency of 3.768995206 Hz. Two rotation cycles are shown for clarity. Error bars indicate the 1σ uncertainty. The grey shaded regions and the blue shaded regions illustrate the off-pulse phase (i.e. DC level) and the on-pulse phase respectively. The pulsed spectrum was obtained by subtracting the DC level from the source spectrum extracted from the on-pulse phase interval.

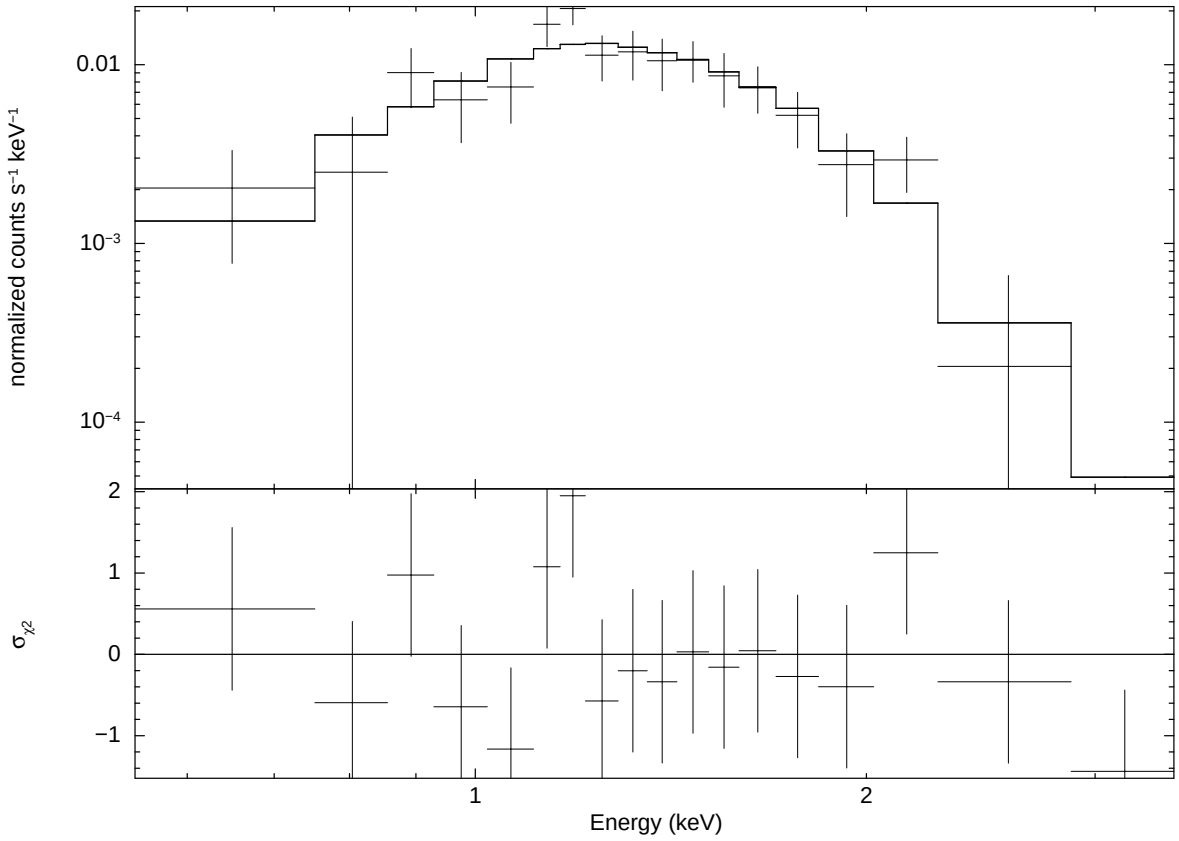

Fig. 6.— The pulsed spectrum of PSR J2021+4026 as observed by *XMM-Newton* PN camera with the best-fit blackbody model illustrated (upper panel) and the contributions to the χ^2 fit statistic (lower panel).

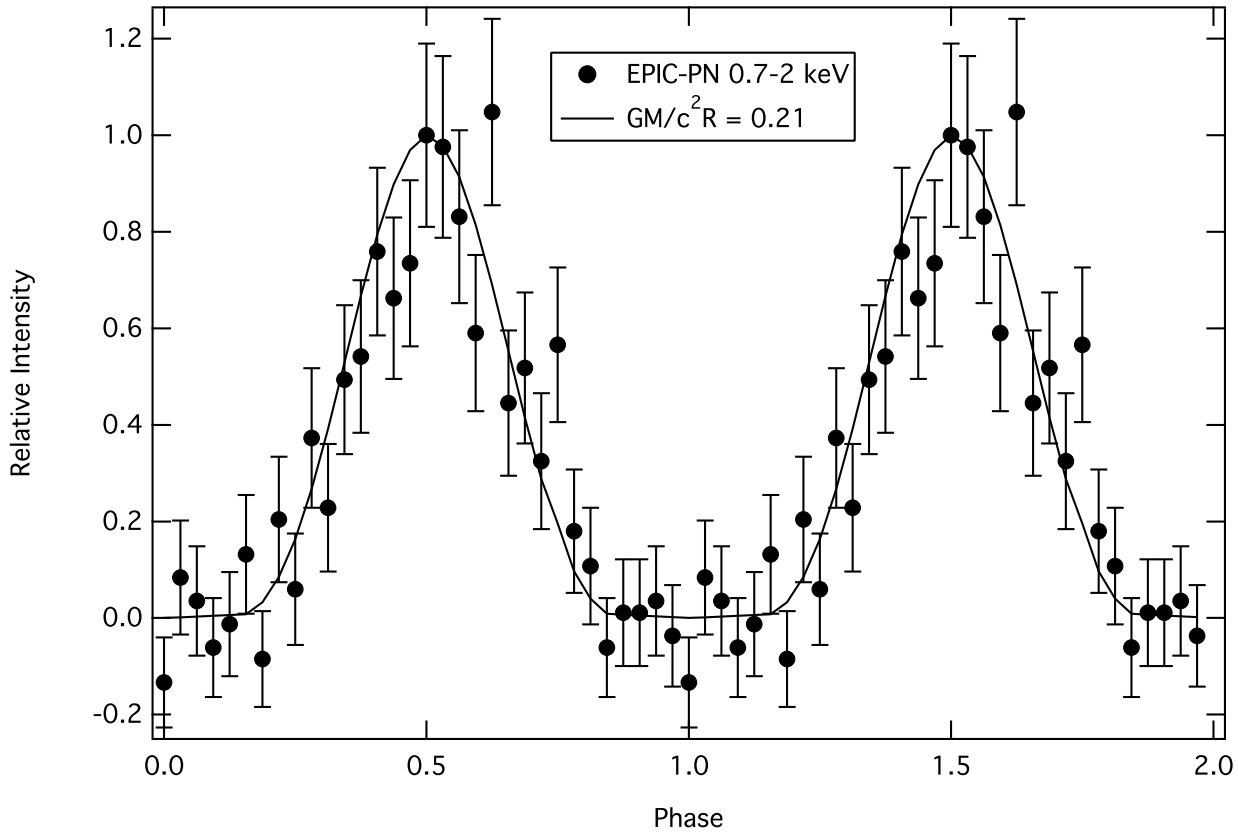

Fig. 7.— The pulse profile of PSR J2021+4026 as observed by *XMM-Newton* PN camera in 0.7-2.0 keV (cf. Fig. 1 in Lin et al. 2013) and the best-fit simulated profile (solid curve) with the effects of gravitational light-bending incoporated. Error bars indicate the 1σ uncertainty. Two rotation cycles are shown for clarity.

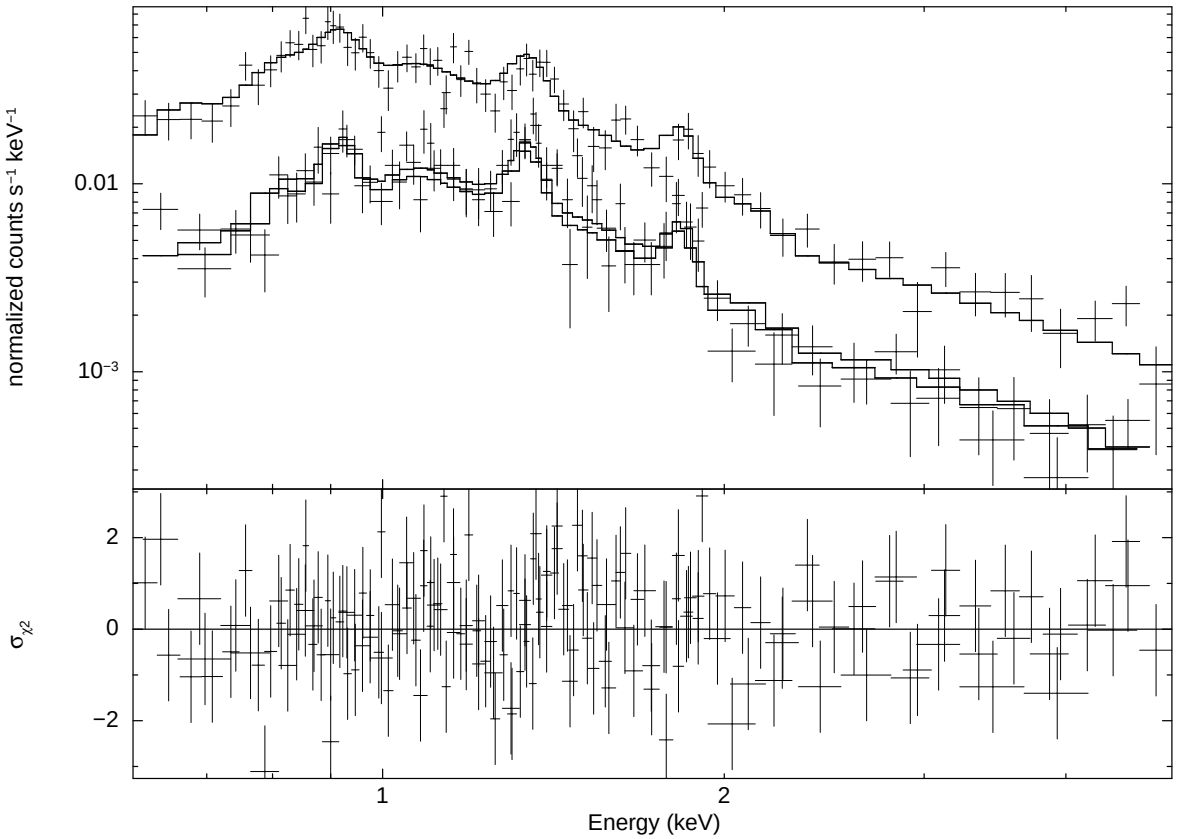

Fig. 8.— Upper panel: X-ray energy spectra of the central region of G78.2+2.1 as observed by MOS1/2 (cf. Fig. 1) and PN (cf. Fig. 2) which are simultaneously fitted to an absorbed non-equilibrium ionization plasma model. Additional power-law components have been applied to account for the residual soft proton contamination in the individual camera. Lower panel: contributions to the χ^2 fit statistic.

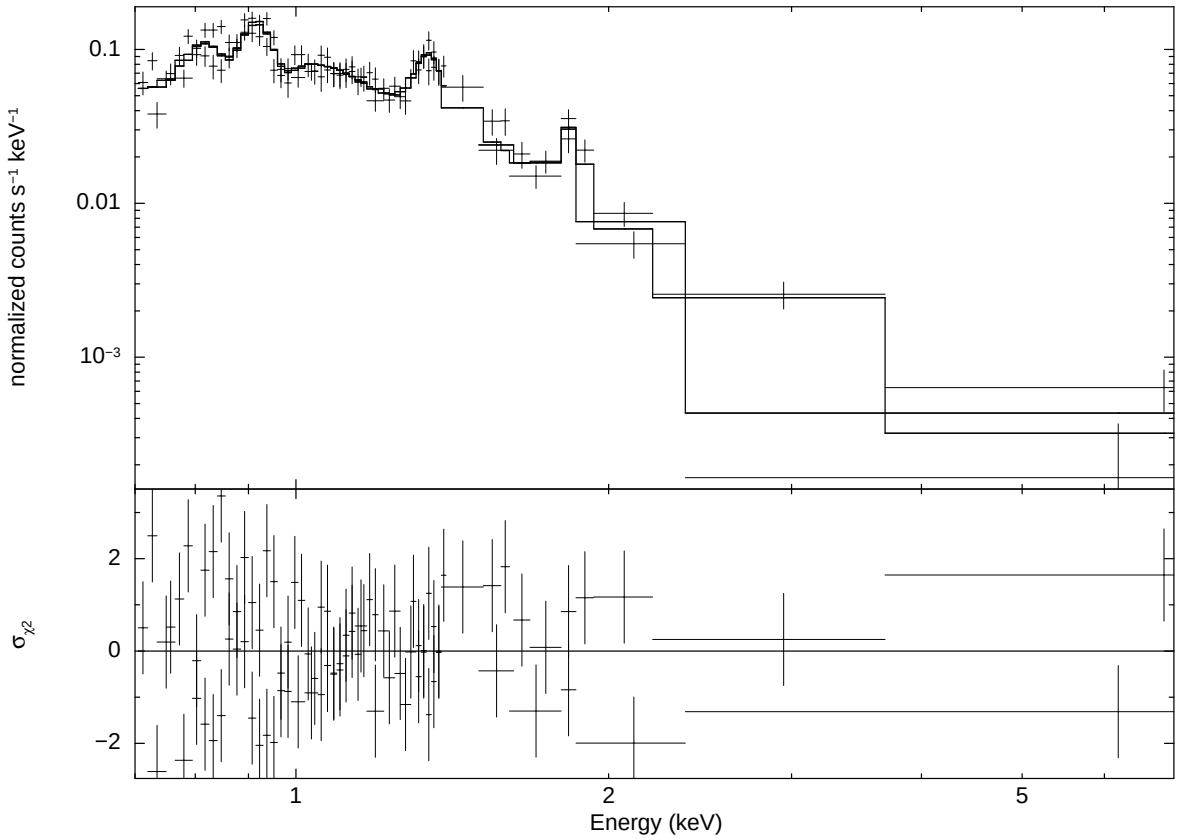

Fig. 9.— Upper panel: X-ray energy spectrum of southeastern region of G78.2+2.1 as observed by MOS1/2 (cf. Fig. 1) which are simultaneously fitted to an absorbed non-equilibrium ionization plasma model. Additional power-law components have been applied to account for the residual soft proton contamination in the individual camera. Lower panel: contributions to the χ^2 fit statistic.

[b]

Table 1:: X-ray sources detected in the southeastern field of G78.2+2.1 as labeled in Figure 1

Source[(a)]	RA (J2000)	DEC (J2000)	$r_{1\sigma}^{(b)}$	Net count rate			Remark[(c)]
				MOS1	MOS2	PN	
No.	(h:m:s)	(d:m:s)	(arcsec)	(cts ks^{-1})	(cts ks^{-1})	(cts ks^{-1})	
1	20:22:21.77	40:31:17.93	0.43	7.11 ± 0.57	7.27 ± 0.60	-	-
2	20:22:15.89	40:28:30.17	0.44	3.01 ± 0.46	3.45 ± 0.39	-	-
3	20:22:09.89	40:29:58.75	0.67	1.06 ± 0.28	1.64 ± 0.28	-	-
4	20:22:02.69	40:26:08.79	0.47	1.17 ± 0.21	1.25 ± 0.30	-	-
5	20:21:58.23	40:30:51.61	0.48	2.93 ± 0.31	2.51 ± 0.29	-	-
6	20:21:57.57	40:26:48.07	0.52	1.25 ± 0.20	1.48 ± 0.23	-	W44
7	20:21:54.78	40:24:34.84	0.69	1.34 ± 0.22	1.38 ± 0.24	-	-
8	20:21:54.65	40:28:55.28	0.21	11.69 ± 0.49	9.83 ± 0.49	-	-
9	20:21:52.95	40:24:19.73	0.78	0.69 ± 0.19	0.77 ± 0.18	-	-
10	20:21:50.50	40:18:32.05	0.55	3.62 ± 0.38	5.37 ± 0.50	-	-
11	20:21:48.07	40:23:40.65	0.77	0.94 ± 0.21	1.10 ± 0.22	-	-
12	20:21:42.89	40:23:54.06	0.72	0.75 ± 0.17	0.66 ± 0.18	-	W38
13	20:21:38.20	40:24:43.18	0.60	1.40 ± 0.19	1.45 ± 0.22	-	W34

14	20:21:38.05	40:29:36.34	0.30	0.88 ± 0.18	1.30 ± 0.22	3.30 ± 0.42	W33
15	20:21:37.18	40:29:58.72	0.32	2.53 ± 0.26	2.50 ± 0.27	7.65 ± 0.52	W32
16	20:21:34.81	40:28:35.74	1.23	0.00 ± 0.00	0.00 ± 0.00	1.34 ± 0.32	W30
17	20:21:33.30	40:29:09.82	0.47	0.86 ± 0.18	1.10 ± 0.25	3.21 ± 0.39	W27
18	20:21:30.48	40:26:46.30	0.22	4.79 ± 0.32	4.45 ± 0.33	12.90 ± 0.64	W20
19	20:21:29.95	40:29:48.68	0.38	1.70 ± 0.23	1.52 ± 0.23	4.89 ± 0.46	W19
20	20:21:20.07	40:17:27.78	0.46	5.52 ± 0.50	5.68 ± 0.55	-	-
21	20:21:11.10	40:28:04.43	0.21	9.13 ± 0.44	7.82 ± 0.43	-	W3
22	20:21:10.21	40:30:53.78	0.55	1.64 ± 0.25	1.97 ± 0.26	-	-
23	20:21:06.54	40:18:44.75	0.49	2.55 ± 0.33	3.23 ± 0.42	-	-
24	20:21:01.74	40:34:42.45	0.38	5.74 ± 0.52	5.06 ± 0.51	-	-
25	20:20:59.24	40:31:42.71	0.63	1.37 ± 0.26	1.24 ± 0.26	-	-
26	20:20:57.37	40:28:27.62	0.34	4.49 ± 0.37	4.42 ± 0.40	-	-
27	20:20:57.01	40:33:26.54	1.10	1.40 ± 0.31	1.11 ± 0.28	-	-
28	20:20:54.62	40:28:21.02	1.10	0.71 ± 0.19	1.12 ± 0.26	-	-
29	20:20:53.15	40:30:24.83	0.51	2.02 ± 0.31	2.23 ± 0.35	-	-
30	20:20:52.33	40:24:29.23	0.29	3.04 ± 0.35	3.54 ± 0.49	-	-
31	20:20:52.09	40:28:26.67	0.46	4.53 ± 0.42	3.61 ± 0.40	-	-
32	20:20:51.11	40:30:31.22	0.84	1.30 ± 0.27	1.32 ± 0.31	-	-
33	20:20:40.65	40:27:03.54	0.40	5.89 ± 0.53	4.51 ± 0.49	-	-

34	20:20:33.41	40:18:25.60	0.69	5.31 ± 0.82	6.74 ± 0.92	-	-
35	20:22:00.96	40:33:41.04	0.89	-	1.33 0.28	-	-
36	20:21:55.92	40:38:31.92	0.85	-	0.84 0.30	-	-
37	20:21:51.36	40:32:30.48	1.31	-	1.48 0.25	-	-
38	20:21:37.44	40:36:40.68	2.40	-	1.10 0.31	-	-
39	20:21:25.44	40:36:14.40	1.53	-	1.33 0.30	-	-
40	20:21:25.20	40:38:15.00	0.78	-	1.37 0.30	-	-
41	20:21:20.16	40:34:55.92	1.28	-	0.68 0.20	-	-
42	20:21:07.20	40:38:53.52	0.74	-	1.29 0.35	-	-

(a) c.f Fig. 1.

(b) 1σ positional uncertainty.

(c) Wx indicates the source detected independently by Weisskopf et al. (2011) with x corresponds to the label in their Fig. 1.

A. Analysis of the X-ray flash-like event XMM J202154.7+402855

In this *XMM-Newton* observation, XMM J202154.7+402855 is detected by MOS1/2 (i.e. source 8 in Fig. 1 and Tab. 1). In examining its light curve, we found that this source is significantly variable and resembles a flash-like event (see Figure 10). A rapid rise of intensity of XMM J202154.7+402855 occured at $\sim$ 40 ks after the start of the investigation at $\sim$ MJD 56028.31. Its count rate increased by a factor of $\sim$ 40 above the quiescent level with a timescale of $\sim$ 1 ks and became the brightest one among all the point sources detected in this observation. After reaching the peak, its count rate returned to the quiescent level in about an hour. In view of its interesting temporal behaviour, we carefully examined timing and spectral properties of this newly detected flash-like event.

In order to probe the spectral behavior of XMM J202154.7+402855, we divided its spectrum into two components: the quiescent spectrum (events in 0–35000 s & 80000–110000 s) and the X-ray flash spectrum (events in 40000–70000 s) [7]. For the quiescent spectrum, we have examined it with various single component model: power-law, blackbody and comptonization of soft photons in a hot plasma (Titarchuk 1994). None of this single component model can provide an acceptable description of the data. We proceeded to fit the quiescent spectrum with composite models. We found that BB+PL can fit the data reasonably well (χ^2=16.3 with 12 d.o.f.), which yields a column density of $N_H = 6.6^{+1.0}_{-1.1} \times 10^{21}$ cm^{-2}, a photon index of $\Gamma = 1.8^{+1.3}_{-1.4}$, a PL normalization at 1 keV of $5.3^{+1.4}_{-1.5} \times 10^{-6}$ photons keV^{-1} cm^{-2} s^{-1}, a blackbody temperature of $kT = 97.2^{+4.3}_{-5.5}$ eV and an emitting radius of $R = 7.8^{+2.4}_{-2.9} d_2$ km. The unabsorbed flux of XMM J202154.7+402855 in the quiescent state is $\sim 9 \times 10^{-13}$ erg cm^{-2} s^{-1} in 0.5-10 keV.

For investigating the X-ray flash spectrum, we further divided it into three stages: a

[7]The time intervals here indicates the time after the start of the investigation

rising stage (events in 40000–41400 s); a rapid declining stage (events in 41400-45000 s) and a slow declining stage (events in 45000-70000 s). For accounting the quiescent contribution in all these segments, we included the BB and PL components in the spectral fits with the parameters fixed at the best-fit values of the quiescent spectrum. In view of the narrow time-windows in dividing these stage, their photon statistics are lower than the quiescent spectrum. In order to minimize the number of free parameters, we also fixed the column absorption at $N_{\rm H} = 6.6 \times 10^{21}$ cm^{-2} as inferred from the quiescent spectrum. On top of the quiescent level, we have added an extra component for modeling the contribution from the flash-like event. We found that an additional comptonized blackbody model (Nishimura et al. 1986; XSPEC model: COMPBB) is capable to yield reasonable spectral fits for all three stages. With the electron temperature of the plasma fixed at 50 keV, the best-fit temperature of the comptonized blackbody for the rising stage, the rapid declining stage and the slow declining stage are found to be $86.9^{+21.0}_{-24.1}$ eV, $103.5^{+13.4}_{-12.8}$ eV and $95.9^{+15.3}_{-14.1}$ eV respectively. The sum of the unabsorbed fluxes in all three stages is $\sim 4 \times 10^{-11}$ erg cm^{-2} s^{-1} in 0.5-10 keV.

Since both burst duration and spectral properties of XMM J202154.7+402855 are inconsistent with a Type-I X-ray burst, we proceeded to consider other possible emission scenarios. We have also explored its temporal behaviour by fitting a power-law model to the fading tail of the event. The results are summarized in Table 2. With all the parameters to be free, the light curve fitting yielded a power-law index of -1.27 ± 0.16 and the best-fit function is shown as the red curve in Fig. 10. Within its 3σ uncertainty, this value is consistent with that of a tidal disruption event (TDE) which has a time dependence of $t^{-5/3}$ (Rees 1988; Phinney 1989; Lodato 2012). With the power-law index fixed at -5/3, the best-fit curve (i.e. blue curve in Fig. 10) also results in a comparable goodness-of-fit.

Considering the possibility of a TDE, we further attempted to search for the quasi-

periodic oscillation (QPO) from the data which has been detected from Swift J1644+57 (Reis et al. 2012). A $\sim$ 200 s QPO has been detected from Swift J1644+57 which is interpreted as the Keplerian frequency of the innermost stable circular orbit of a supermassive black hole (Reis et al. 2012). Motivated by this discovery, we searched for the periodic signal from XMM J202154.7+402855 in a range from 0–400 s centered at 200 s with a resolution of 0.1 s by χ^2 test. The highest peak obtained from the periodogram is at 115.1 s with χ^2_{15} less than 3. Even we only considered those events obtained between the main outburst of 40000–55000 s shown in Fig. 10, the similar result of the $\chi^2_{15} = 3.2$ was detected at a trial period of 115 s. We also considered to detect the periodic signal using the Lomb-Scargle method (Scargle 1982) on light curves rebinned with 20 s and 40 s. With this method, we concluded that there is no periodicity can be detected with a power more significant than 90% confidence level. Our analysis indicates that there is no stable periodic signal can be detected from the current observation.

Since QPO might appear intermittently or varies with time, these make the aforementioned periodicity search for the whole light curve difficult. In view of this, we have also searched the possible periodic signal by computing the dynamic power spectrum (Clarkson et al. 2003a,b). We adopted a window size of 1000 s which is approximately the duration of the flash-like event. In order to depress the effect of the trend, we used the empirical mode decompositoin (Huang et al. 1998) to filter the trend and only the de-trended light curve was examined by the dynamical power spectrum. However, there is no significant signal of QPO can be detected from the dynamic Lomb-Scargle periodogram. Together with the non-detection of any periodic signal, the fact that the burst duration of XMM J202154.7+402855 is far shorter than a typical TDE which lasts for a timescale of months (e.g. Reis et al. 2012) does not favor this scenario.

Another possible source nature of XMM J202154.7+402855 is a flaring early-type

star. This requires a search for the optical counterpart for constraining its properties. Utilizing the USNO-B1.0 catalog (Monet et al. 2003), we have identified a bright source, USNO-B1.0 1304-0388936, locates at $\sim$ 3" away from the nominal X-ray position of XMM J202154.7+402855 with magnitudes of $B = 14.48$, $R = 13.65$ and $I = 12.85$. Assuming it is the optical counterpart of XMM J202154.7+402855, its X-ray-to-optical flux ratio is $f_x/f_{opt} \sim 10^{-3}$ during quiescence which is quite typical for a field star (Maccacaro et al. 1988). To investigate if the positional offset between the X-ray source and the optical counterpart is a result of proper motion, we have also checked the UCAC3 catalog (Zacharias et al. 2010). The source 3UC 261-199420 in UCAC3 has its nominal position differed from USNO-B1.0 1304-0388936 only by ~ 0.5" and its proper motion is very small: $\mu_{\rm RA} = 1.9$ mas/yr and $\mu_{\rm Dec} = -0.9$ mas/yr. Calculating the angular shift from the central epoch for the position given by UCAC3 to the epoch of our *XMM-Newton* observation, we found that it only moves by ~ 31 mas. Hence, the offset between XMM J202154.7+402855 and the optical source cannot be reconciled by the proper motion. Although the positional offset is comparable to the absolute point accuracy of *XMM-Newton* [8], further investigation is required for securing the association between XMM J202154.7+402855 and the optical source.

[8]see http://xmm.esac.esa.int/external/xmm_user_support/documentation/uhb_2.1/node108.html

Table 2: Best-fit parameters with both free/fixed power-law indices in $y = a_1 + a_2 \times (t - a_3)^{a_4}$ to the tail of X-ray flash

Parameters	a_1 (cts/s)	a_2	a_3 (s)	a_4	χ^2_ν $(d.o.f)$
a_4 free	0.01	1511 ± 2074	40950 ± 215	-1.27 ± 0.16	1.099(62)
a_4 fixed	0.01	49112 ± 5128	40388 ± 121	-5/3	1.117(63)

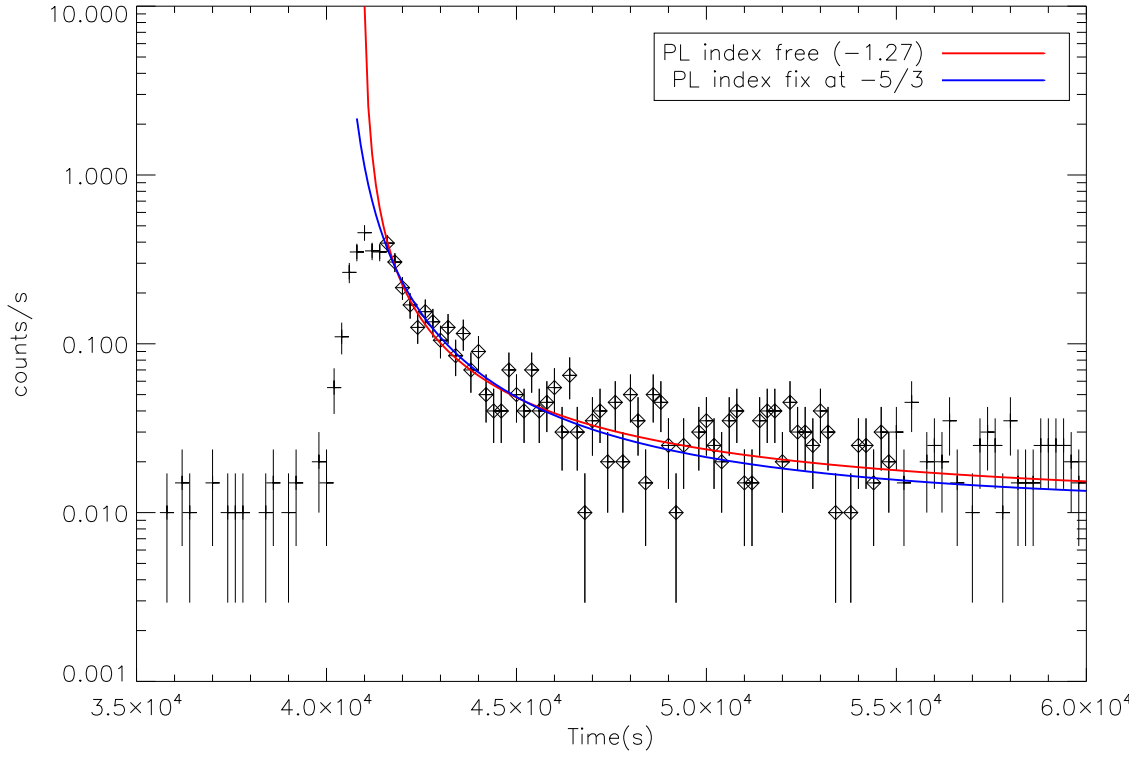

Fig. 10.— A flash light curve of XMM J202154.7+402855 obtained from MOS 1/2. The epoch zero of the merged light curve corresponds to MJD 56028.31 related to the selected GTI of *XMM* archive investigated in 2012. The light curve of XMM J202154.7+402855 was binned with 200 s labelled by cross signs. The highest peak reaches to ~ 0.4 cts/s, and all the error bars of data points indicate the 1σ uncertainty. Data points labelled by diamonds demonstrate the cooling tail of the burst, and the red and blue lines are the best fits to a power-law model with a free index and a fixed index at -5/3, respectively. All the obtained parameters are presented in Table 2.

REFERENCES

Abdo, A. A., et al. 2013, ApJS, 208, 17

Abdo, A. A., et al. 2010, ApJS, 187, 460

Abdo, A. A., et al. 2009a, ApJS, 183, 46

Abdo, A. A., et al. 2009b, Science, 325, 840

Aliu, E., et al. 2013, ApJ, 770, 93

Allafort, A., et al. 2013, ApJ, 777, L2

Becker, W., et al. 2004, ApJ, 615, 897

Cheng, K. S., Taam, Ronald E., & Wang, W. 2004, ApJ, 617, 480

Cheng, K. S., & Zhang, L. 1999, ApJ, 515, 337

Chevalier, R. A. 2000, ApJ, 539, L45

Clarkson, W. I., Charles, P. A., Coe, M. J., & Laycock, S. 2003a, MNRAS, 343, 1213

Clarkson, W. I., Charles, P. A., Coe, M. J., Laycock, S., Tout, M. D., & Wilson, C. A. 2003b, MNRAS, 339, 447

Downes, D., & Rinehart, R. 1966, ApJ, 144, 937

Gaensler, B. M. 2005 AdSpR, 35, 1116

Gaensler, B. M., et al. 2004, ApJ, 616, 383

Goldreich, P., & Julian, W. H. 1969, ApJ, 157, 896

Green D.A., 2009, BASI, 37, 45

Hansen, M. S., & Phinney, E. 1997, MNRAS, 291, 569

Hobbs, G., Lorimer, D. R., Lyne, A. G., & Kramer, M. 2005, MNRAS, 360, 974

Huang, N. E., Shen, Z., Long, S. R., Wu, M. C., Shih, H. H., Zheng, Q., Yen, N.-C., Tung, C. C., & Liu, H. H. 1998, RSPSA, 454, 903

Huang, R. H. H., Wu, J. H. K., Hui, C. Y., Seo, K. A., Trepl, L., & Kong, A. K. H. 2014, ApJ, 785, 118

Hui, C. Y., Huang, R. H. H., Trepl, L., Tetzlaff, N., Takata, J., Wu, E. M. H., & Cheng, K. S. 2012, ApJ, 747, 74

Hui, C. Y., & Becker, W. 2008, A&A, 486, 485

Hui, C. Y., & Becker, W. 2007, A&A, 467, 1209

Hui, C. Y., & Cheng, K. S. 2004, ApJ, 608, 935

Leahy, D. A., Green, K., & Ranasinghe, S. 2013, MNRAS, 436, 968

Li, J. Q., et al. 2004, ApJ, 610, 1204

Lin, L. C. C., et al. 2013, ApJ, 770, L9

Lodato, G. 2012, in European Physical Journal Web of Conferences, Vol. 39, European Physical Journal Web of Conferences, 1001

Lozinskaya, T. A., Pravdikova, V. V., & Finoguenov, A. V. 2002, AstL, 28, 223

Maccacaro, T., Gioia, I. M., Wolter, A., Zamorani, G., & Stocke, J. T. 1988, ApJ, 326, 680

Monet, D., et al. 2003, AJ, 125, 984

Nishimura, J., Mitsuda, K., & Itoh, M. 1986, PASJ, 38, 819

Pechenick, K. R., Ftaclas, C., & Cohen, J. M. 1983, ApJ, 274, 846

Phinney, E. 1989, the Center of the Galaxy (IAU Symp. 136), ed. M. Morris

Ray, P. S., et al. 2011, ApJS, 194, 17

Rees, M. J. 1988, Nature, 333, 523

Reis, R. C., et al. 2012, Science, 337, 949

Scargle, J. D. 1982, ApJ, 263, 835

Titarchuk, L. 1994, ApJ, 434, 570

Trepl, L., et al. 2010, MNRAS, 405, 1339

Uchiyama, Y., Takahashi, T., Aharonian, F. A., & Mattox, J. R. 2002, ApJ, 571, 866

Vink, J. 2012, A&ARv, 20, 49

Weisskopf, M., et al. 2011, ApJ, 743, 74

Zacharias, N., et al. 2010, AJ, 139, 2184

This manuscript was prepared with the AAS LaTeX macros v5.0.